

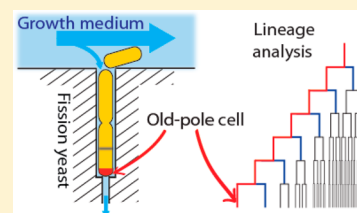
# 3D-Printed Microfluidic Microdissector for High-Throughput Studies of Cellular Aging

Eric C. Spivey,<sup>†,||</sup> Blerta Xhemalce,<sup>†,§</sup> Jason B. Shear,<sup>\*,‡,§</sup> and Ilya J. Finkelstein<sup>\*,†,§,||</sup>

<sup>†</sup>Department of Molecular Biosciences, <sup>‡</sup>Department of Chemistry and Biochemistry, <sup>§</sup>Institute for Cellular and Molecular Biology, <sup>||</sup>Center for Systems and Synthetic Biology, The University of Texas at Austin, Austin, Texas 78712, United States

## Supporting Information

**ABSTRACT:** Due to their short lifespan, rapid division, and ease of genetic manipulation, yeasts are popular model organisms for studying aging in actively dividing cells. To study replicative aging over many cell divisions, individual cells must be continuously separated from their progeny via a laborious manual microdissection procedure. Microfluidics-based soft-lithography devices have recently been used to automate microdissection of the budding yeast *Saccharomyces cerevisiae*. However, little is known about replicative aging in *Schizosaccharomyces pombe*, a rod-shaped yeast that divides by binary fission and shares many conserved biological functions with higher eukaryotes. In this report, we develop a versatile multiphoton lithography method that enables rapid fabrication of three-dimensional master structures for polydimethylsiloxane (PDMS)-based microfluidics. We exploit the rapid prototyping capabilities of multiphoton lithography to create and characterize a cell-capture device that is capable of high-resolution microscopic observation of hundreds of individual *S. pombe* cells. By continuously removing the progeny cells, we demonstrate that cell growth and protein aggregation can be tracked in individual cells for over ~100 h. Thus, the fission yeast lifespan microdissector (FYLM) provides a powerful on-chip microdissection platform that will enable high-throughput studies of aging in rod-shaped cells.



The relative simplicity and ease of genetic manipulation in yeasts have propelled their adoption as popular model organisms for aging research. In 1959, Mortimer and Johnston reported that in *S. cerevisiae* the replicative lifespan (RLS), the number of daughters produced by a mother before it dies, is limited to approximately 30 generations.<sup>1</sup> Since that seminal observation, most studies have focused on replicative aging in *S. cerevisiae* as a genetically tractable model system for aging in mitotically active cells.<sup>2–6</sup> Many of the mechanistic and genetic insights gained from these replicative aging studies have since been explored in metazoans, cementing the importance of unicellular eukaryotes in aging research.<sup>6–8</sup>

To determine the RLS of individual cells, progeny must be continuously removed from the mother cell. This is typically accomplished by manual manipulation of the cells under a low magnification dissecting microscope, a method that has not changed appreciably in the last 50 years.<sup>1,9</sup> Although conceptually simple, microdissection RLS assays are laborious and time-consuming, precluding a detailed analysis of aging phenotypes.<sup>10</sup> In addition, constant repositioning of the cells on agar plates is incompatible with continuous microscopic observation. As the cells are moved onto different areas of a plate, changes in the local nutrient environment may also introduce extrinsic heterogeneity into the RLS measurement.

Although aging in *S. cerevisiae* has been intensely studied for over 50 years, little is known about replicative aging in the distantly related fission yeast *Schizosaccharomyces pombe* (*S. pombe*). As *S. pombe* divides by medial fission, the replicative age of a cell can be defined as the age of the oldest cell pole.<sup>10,11</sup> Early studies suggested that *S. pombe* has a short (~15 generation) RLS.<sup>10,11</sup> However, a recent report concluded that,

under ideal growth conditions, *S. pombe* avoids replicative aging and achieves functional immortality.<sup>9</sup> These diverging results may partially stem from the difficulty of studying *S. pombe* replicative aging via manual micromanipulation. Identifying the old-pole cells amidst new-pole progeny is particularly challenging.<sup>10,11</sup> The low-throughput nature of traditional microdissection studies also precludes a detailed mechanistic and genetic analysis of the factors that may contribute to replicative aging in *S. pombe*.

Microfluidic platforms offer a powerful approach for capturing and observing individual cells.<sup>12–21</sup> Microfluidic devices have been used to investigate the mechanical properties of *S. pombe* cells,<sup>15,16,22</sup> to apply rapid changes in growth temperature,<sup>23,24</sup> and to observe synchronized cohorts of cells.<sup>18,25</sup> In conventional microfluidic device fabrication, the first step in producing a master structure is to photocure a polymer through a high-resolution UV mask.<sup>26</sup> A polydimethylsiloxane (PDMS) flowcell is then molded around the master structure to generate the microfluidic device.<sup>27</sup> However, fabrication of three-dimensional (3D) master structures with micrometer-scale features is a major bottleneck for rapid device prototyping. Producing multiple high-resolution (<10  $\mu\text{m}$  feature size) photomasks for each prototype iteration is time-consuming and can be prohibitively expensive. Moreover, aligning and exposing sequential layers of

Received: March 10, 2014

Accepted: July 4, 2014

Published: July 4, 2014

photoresist makes the fabrication of multilayer master structures challenging.

In this report, we describe a multiphoton lithography fabrication approach that combines raster scanning of a laser beam on a dynamic mask with synchronized microscope stage movement to produce millimeter-sized 3D master structures for microfluidics. Using this flexible strategy for  $\mu$ 3D-printing ( $\mu$ 3DP), we designed and optimized the fission yeast lifespan microdissector (FYLM), a microfluidic device that is capable of capturing and retaining individual fission yeast cells. As the cells divide, the progeny are continuously removed, permitting continuous,  $\sim$ 100 h microscopic observation of individually addressable old-pole cells. In addition, we demonstrate that the FYLM enables the fluorescent observation of aggregate dissolution after the induction of a proteotoxic stress. Thus, the FYLM promises to open new avenues for studying aging and other long-term processes in *S. pombe* and other rod-shaped organisms.

## ■ EXPERIMENTAL SECTION

**Fabrication of PEG Masters.** A 20 mM HEPES (L6876, Sigma) buffered saline (HBS) solution containing 100 mM NaCl (buffered to pH 7.3) was prepared as a solvent for the precursor solution. Rose Bengal (RB, 330000, Aldrich) was used as the photosensitizer for multiphoton lithography. Fifteen mg of RB was added to 110  $\mu$ L of HBS and 375 mg of 700 Da polyethylene glycol diacrylate (PEGDA, Aldrich 455008) so that the final mass percentage of PEGDA was 75% (Note: All following percentages represent the mass of the stated solute divided by the mass of the solution (w/w)  $\times$  100%, unless otherwise noted.) and the final mass percentage of RB was 3%. Two parallel 25 mm  $\times$  2 mm strips of double-sided tape (Scotch tape, 3M) were placed  $\sim$ 15 mm apart along the long side of an acrylated glass slide (CEL Associates). A 22 mm  $\times$  40 mm, #0 coverglass (Fisher) was placed over the strips and affixed with gentle pressure. Twenty  $\mu$ L of the PEGDA/RB solution was loaded into the space between the slide and the coverglass using capillary action. This assembly was then placed with the coverglass facing down on the stage of an inverted microscope (Zeiss Axiovert 135) used for  $\mu$ 3DP. We found that PEGDA/RB was an excellent fabrication material for multiple rounds of PDMS casting (see Supporting Information).

The long-scan  $\mu$ 3DP apparatus described in this manuscript is based on an earlier version of the instrument that has been described in detail elsewhere.<sup>28</sup> Briefly, the collimated output beam of a mode-locked titanium:sapphire laser, tuned to 740 nm (Coherent Mira 900F), was focused onto an electrically actuated scan mirror that scanned the beam in a linear pattern through a series of lenses onto a 800  $\times$  600 (SVGA) digital micromirror device (DMD), obtained from a BenQ MP510 projector. The DMD was controlled by a computer displaying binary mask images, where micromirrors on the DMD corresponding to the white pixels of the mask image directed the beam into the back aperture of a 40 $\times$  (0.95 NA) Zeiss Fluor microscope air objective. Thus, only the areas of the focal plane corresponding to the white areas of the mask resulted in photo-cross-linking within the PEGDA precursor solution. Three-dimensional objects were fabricated in a layer-by-layer process by coordinating the movement of the microscope stage with the micromirrors on the DMD. The stage movements and DMD mirrors were controlled by custom software written in LabView (National Instruments, software available upon request).

The average laser power was adjusted using a half-wave plate/polarizer pair to provide 20–30 mW at the back aperture of the objective. The linear scan was established to generate a fast-axis (“x-axis”) scan velocity of  $\sim$ 7 mm s<sup>-1</sup>, while the orthogonal (“y-axis”) stage movement velocity was set at 20  $\mu$ m s<sup>-1</sup>. These relative scan speeds were selected so that the lines of cross-linked PEGDA overlapped to produce a continuous three-dimensional PEGDA object. Our FYLM structures were 0.44 mm long, consisted of 20 z-layers spaced 0.5  $\mu$ m apart, and took approximately 12 min to fabricate (Figure S3, Supporting Information). The fabrication time was predominantly determined by the y-axis stage movement. Additional capabilities of our new long-scan  $\mu$ 3D printing approach are summarized in the supplemental discussion, Supporting Information.

**Scanning Electron Microscopy.** PEGDA master structures were imaged using a Zeiss Supra 40 VP scanning electron microscope. The PEGDA structures were prepared for scanning electron microscopy (SEM) by sequential 15 min washes with 20 mL each of deionized water, ethanol, and methanol. After the methanol was removed, structures were placed in a drying oven at 60  $^{\circ}$ C for 5 min. The structures were then sputter coated with a 10 nm layer of Pt–Pd alloy using a Cressington 208 benchtop sputter coater for analysis in the SEM.

**Fabrication of Microfluidic Flowcells.** Glass coverslips (Fisher; 22-266-822) were washed with 2% liquid detergent (Hellmanex III; Helma Analytics) followed by rinsing with water and isopropanol before drying at 60  $^{\circ}$ C on a hot plate. PDMS prepolymer and hardener (Dow Sylgard 184) were mixed at a 10:1 weight ratio for 30 min on a rotating mixer. The mixed polymer was then centrifuged at 1500 rpm for 90 s to remove large air bubbles. Master structures were placed in a shallow container and covered with  $\sim$ 5 g of liquid PDMS. The filled container was placed in a vacuum chamber and degassed under vacuum ( $\sim$ 630 mmHg) for  $\sim$ 15 min to remove air bubbles. The PDMS was poured over the PEGDA master or SU-8 remaster (see the supplemental methods, Supporting Information) to a depth of  $\sim$ 1 mm. After curing in a 60  $^{\circ}$ C oven for 1 h, nanoports (IDEX Corporation; N-333) were placed on top of the interface inlets and an additional  $\sim$ 2 mm of PDMS was used to cement the nanoports in place. PDMS was then cured for an additional 3 h, after which the PDMS microfluidic device was separated from the master and trimmed to create a flat surface for plasma bonding. A 1 mm biopsy-punch (Acu-Punch, Accuderm) was used to make through-holes between the nanoport and the microfluidic device. PDMS devices were treated in an air plasma cleaner (Harrick Scientific) for 20 s and immediately bonded to the freshly cleaned coverslips. PDMS flowcells were used within a few days of fabrication.

**Loading Microfluidic Flowcells with *S. pombe*.** Figure S4, Supporting Information, summarizes the microfluidic layout used to connect the FYLM to the syringe pump and injection loop. To load the device, *S. pombe* cells were grown overnight in YES medium (Sunrise Science Products) to an OD<sub>600</sub> < 1.0 at 30  $^{\circ}$ C and then maintained in mid log growth prior to loading into the FYLM. Cells were loaded into the device using a two-channel syringe pump (Legato 210, KD Scientific) according to the loading scheme described in Figure S4 and the supplemental methods, Supporting Information. Briefly,  $\sim$ 10  $\mu$ L of the cell solution was injected into the flowcell manually. After flushing the device to remove excess cells not caught in catch channels, time-lapse image acquisition was

initiated and the flow rate was maintained at  $1\text{--}2\ \mu\text{L}\ \text{min}^{-1}$ . Table S1, Supporting Information, summarizes the strains used in this study.

**Single-Cell Microscopy and Data Analysis.** All microscopy was performed using an objective-type inverted microscope (Nikon Eclipse TE2000) equipped with a motorized microscope stage (Prior ProScan II). Images were collected with a  $40\times$  or  $60\times$  air 0.95 numerical aperture objective (Nikon CFI Plan Apo  $\lambda$ ) using standard bright field (Köhler) illumination. Fluorescence excitation was accomplished using a xenon arc lamp (Sutter Instruments Lambda LS) and a standard GFP filter set (Chroma ET490/20 $\times$ , 89100bs, ET525/36m). Images were acquired using a back-thinned EM-CCD (Photometrics Cascade II 512) controlled by NIS-Elements software (Nikon) and processed using ImageJ (<http://rsbweb.nih.gov/ij/>). For live-cell tracking, images were captured every 2 min. Data analysis was performed in ImageJ, MATLAB (MathWorks), and Microsoft Excel. Cell doubling times were scored by manually observing the formation of the division septum between two cells. Cell lengths were manually measured using the ImageJ ROI function. All reported error bars correspond to the standard deviation of the indicated number of individual cell measurements. The *p*-values reported in Figures 6 and 7 were computed in MATLAB. Figure 6C was analyzed using a two-tailed paired *t* test, and Figure 7 was analyzed using a two-tailed, two-sample *t* test without assuming equal variance.

## RESULTS AND DISCUSSION

**Long-Scan  $\mu\text{3D}$ -Printing.** Multiphoton lithography is a powerful tool for rapidly fabricating micrometer-scale 3D structures in a variety of materials.<sup>29–36</sup> However, generating millimeter-scale, arbitrary 3D structures remains a key challenge. Fabrication of structures that are larger than the optical field-of-view (typically  $\sim 250\ \mu\text{m}$  for a  $40\times$  objective) can be accomplished by manually tiling multiple fields-of-view.<sup>28</sup> Tiling two or more fields can lead to misalignments or double exposure, which may cause unpredictable voids and ridges in the 3D structure. In another approach, SU-8 substrates on a programmable microscope stage are translated in 3D, allowing the rapid fabrication of millimeter- to centimeter-scale structures.<sup>37,38</sup> Below, we describe a new method that combined elements of each of these approaches to rapidly fabricate continuous millimeter-scale devices with arbitrary 3D geometries.

To generate millimeter-scale devices with high-aspect-ratio features, we developed a complementary “long-scan”  $\mu\text{3D}$ DP method that integrates rapid, dynamic mask laser scanning with millimeter-scale stage scanning (Figure 1). The long-scan  $\mu\text{3D}$ DP method combines the flexibility of dynamic mask-based  $\mu\text{3D}$  printing<sup>28,35,39</sup> with the millimeter-length scales achieved by previous raster-scan methods.<sup>37,38</sup> The focused output of the fabrication laser is linearly scanned over a digital micromirror device (DMD), which displays a timed sequence of digital masks. Presentation of masks on the DMD is coordinated with movement of the microscope stage along an axis orthogonal to the linear laser scan (Figure 1 and Video S1 (ac500893a\_si\_002.avi), Supporting Information). This method can be used to fabricate millimeter-scale 3D structures with micrometer-sized features. A more detailed discussion of the capabilities of this system is included in the supplemental methods, Supporting Information.

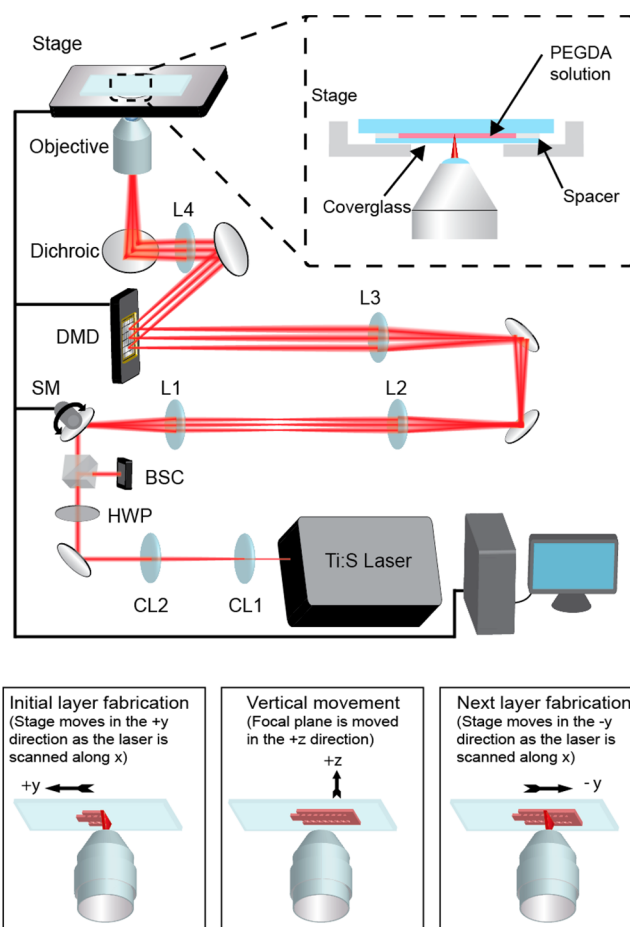


**Figure 1.** Long-scan  $\mu\text{3D}$ DP. (top) Configuration of optical components. The output of a femtosecond titanium:sapphire (Ti:S) laser is collimated by lenses CL1 and CL2 before passing through a half-wave plate (HWP) and beam-splitting cube (BSC). The beam is linearly scanned by a scanning mirror (SM) and then passed through two pairs of lenses (L1–L4) that expand both the beam diameter and the scan pattern. Between L3 and L4, the beam is focused on the DMD. Light reflecting from specified DMD mirrors is directed into the back aperture of a high-NA objective and focused into the PEGDA solution. Inset: PEGDA solution is introduced by capillary action into a space between a coverglass and a glass slide. The scanning mirror, DMD, and microscope stage are coordinated by a computer. (bottom) A sequence of timed mask instructions is sent to the DMD in coordination with lateral movement of the stage, producing a single long structure with micrometer-scale features. At the end of lateral movement, the stage is stepped along the optical axis to fabricate the next device layer.

We used polyethylene glycol diacrylate (PEGDA) to fabricate  $\sim 0.5\ \text{mm}$ -long FYLM master structures. Use of a solution of photosensitizer and PEGDA provided several advantages compared to fabrication using SU-8 (see supplemental methods, Supporting Information). PEGDA structures were chemically inert, permanently bonded to the substrate, and refractory to swelling under alcohol and aqueous buffer conditions. Furthermore, PEGDA structures could be reused to cast multiple PDMS devices. Thus, long scan  $\mu\text{3D}$ DP in PEGDA offers a robust approach for rapidly generating large-scale 3D structures for downstream microfluidics applications.

**Microfluidic Microdissector for Fission Yeast.** We designed a series of FYLM master structures for capturing and retaining individual fission yeast cells in a PDMS-based

microfluidic device (Figures 2 and S3, Supporting Information). The rod-like haploid fission yeast cells are typically  $\sim 14 \mu\text{m}$

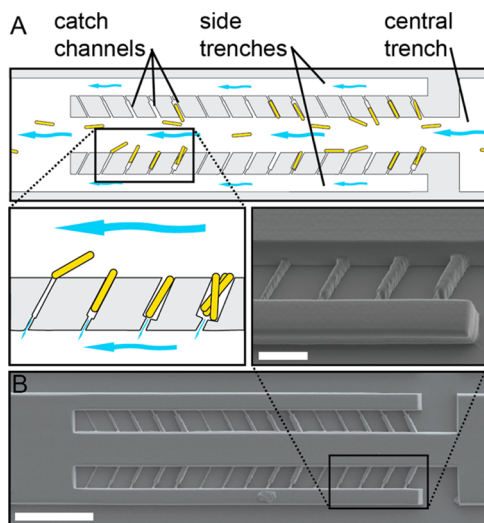


**Figure 2.** Schematic of fission yeast lifetime microdissector (FYLM). (A) Cells in solution enter the device through a central trench. Flow is from right to left (illustrated with blue arrows). Side trenches allow flow through the catch channels, drawing cells into the channels and retaining them via suction. Detail: Illustration of how catch channel width affects cell loading. (B) PEGDA master structure used to generate a PDMS device with variable catch channel dimensions. Scale bar is  $100 \mu\text{m}$ . Detail: Higher magnification image of the master structure showing (from left to right) 3, 4, 5, and  $6 \mu\text{m}$  catch channels. Scale bar is  $20 \mu\text{m}$ .

long before division and  $\sim 7 \mu\text{m}$  long after division (at “birth”) and  $4 \mu\text{m}$  wide. Cells are loaded into the device via a wide ( $40 \mu\text{m}$ ) central trench, and individual cells are retained in narrow side channels. A  $2 \mu\text{m}$ -wide constriction at the bottom of each channel opens into a  $20 \mu\text{m}$  side trench, creating a drain while preventing the  $\sim 4 \mu\text{m}$ -wide cells from slipping out (Figure S2, Supporting Information). A pressure gradient between the central and side trenches provides mild suction that helps to retain cells for long-term analyses, and provides a constant flow to supply nutrients and remove waste. As *S. pombe* divides by medial fission, progeny cells grow to fill the catch channels and are eventually washed away by a continuous perfusion of fresh growth media (Video S2 (ac500893a\_si\_003.avi), Supporting Information).

Efficient loading, capture, and long-term retention of cells within the catch channels are critically dependent on the relative dimensions of the trenches and catch channels (illustrated in Figure 2A). To optimize the FYLM device, we exploited  $\mu\text{3DP}$  to prototype several experimental master structures (Figures 2 and S3, Supporting Information). Figure 2B shows an SEM image of a master structure where the catch channel dimensions are sequentially varied from  $2 \times 2 \mu\text{m}$  to  $6 \times 6 \mu\text{m}$  (width  $\times$  height). Producing this master structure via conventional soft lithography would be prohibitively difficult, as it would require the fabrication and precise (submicrometer-scale) alignment of at least five unique UV photomasks.

PDMS was cured around the master structure to construct a microfluidic device (Figure S1, Supporting Information). To characterize cell loading and retention, exponentially dividing fission yeast cells were flushed through the device. A precision syringe pump maintained accurate, pulse-free media flow. As

expected, nearly all of the  $6 \mu\text{m} \times 6 \mu\text{m}$  (width  $\times$  height) channels were filled with cells. However,  $\sim 90\%$  of these channels captured two or more cells side-by-side, precluding a simple analysis of the replication dynamics of each cell. Four  $\mu\text{m}$ -wide catch channels offered the best balance between efficient single-cell loading and retention (Figure 3), as  $3 \mu\text{m}$ -

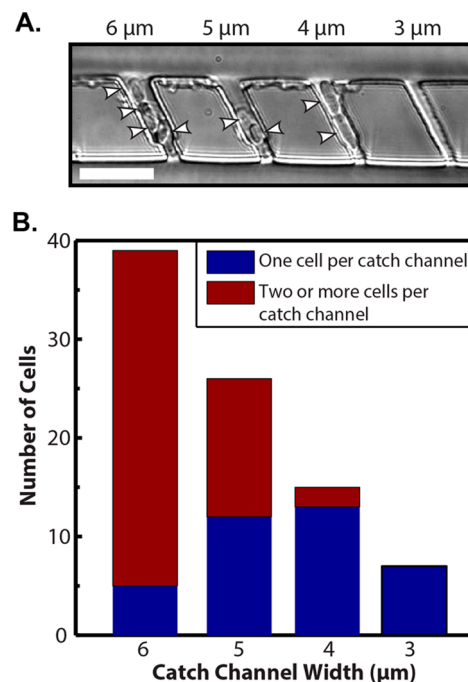


**Figure 3.** (A) A bright field image showing *S. pombe* cells filling catch channels of variable dimensions. The white arrowheads point to individual cells. The  $6 \mu\text{m}$ -wide (nominal) channel (left) and  $5 \mu\text{m}$ -wide channel (second from left) have both captured more than one cell side-by-side, making lineage tracking difficult. The  $4 \mu\text{m}$ -wide channel caught a single cell that divided. At division, wild type fission yeast cells are, on average,  $\sim 14 \mu\text{m}$  long and  $\sim 4 \mu\text{m}$  wide. The scale bar is  $25 \mu\text{m}$ . (B) Cell loading was quantified for catch channels of various widths. The graph represents the distribution of cells caught in 24 channels of a given width. As expected,  $4 \mu\text{m}$ -wide channels offered the best compromise for capturing individual cells with a high loading efficiency.

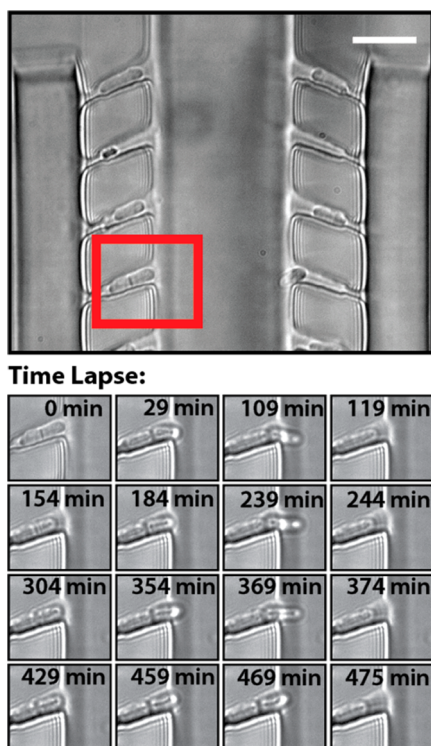
wide channels were too narrow to load cells reliably and  $2 \mu\text{m}$ -wide channels did not load any cells. Thus,  $4 \mu\text{m}$ -wide catch channels were used in all subsequent devices. Next, we characterized the loading efficiency as a function of the angle between the catch channel and the central trench. We tested three devices with  $45^\circ$ ,  $60^\circ$ , and  $90^\circ$  angles (Figure S3, Supporting Information). We observed that typically  $\sim 50\%$  of the catch channels could be reproducibly loaded with cells in all three configurations. We anticipate that refinements to the loading protocol may ultimately increase the percentage of catch channels filled.

The morphology of individual *S. pombe* cells can vary drastically in different genetic backgrounds, potentially requiring further optimization of the FYLM catch channel dimensions. For example, a recent genome-wide deletion mutant screen identified 513 genes that led to an elongated cell phenotype, suggesting a defect in cell cycle progression.<sup>40</sup> In addition, 25 mutants exhibited a small-cell morphology.<sup>40,41</sup> Of these, the *wee1* deletion strain had the most severe phenotype, dividing at half the length of wild type cells ( $7 \mu\text{m}$ -

long at cell division).<sup>41</sup> The variable catch channel device described above will be essential for determining the optimal catch channel geometry for diverse cell morphologies.

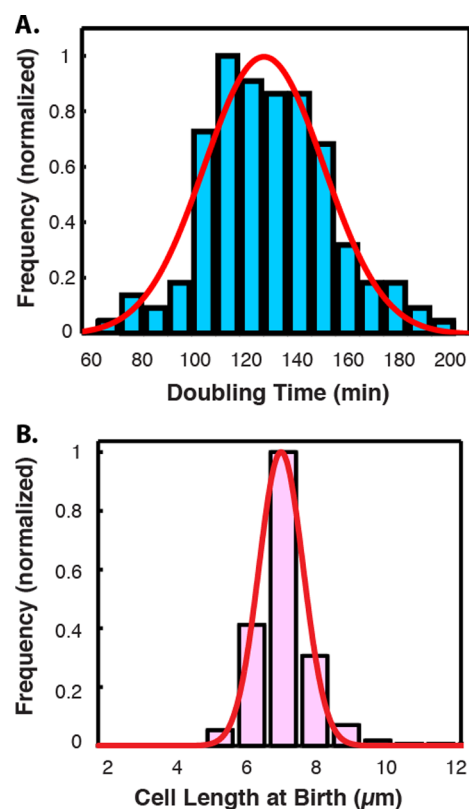
**Continuous, Long Time-Scale Observation of Fission Yeast.** To observe the replication dynamics of individual fission yeast cells, we maintained devices at  $31 \pm 1$  °C using a temperature-controlled atmospheric chamber. To observe cells along the full FYLM device, multiple fields-of-view were acquired by scanning the motorized microscope stage. A bright field image was acquired in 2 min intervals at each stage position.

Figure 4 demonstrates a single *S. pombe* cell dividing over four generations. As expected, the cell is retained within the



**Figure 4.** Monitoring cell growth in the FYLM. (top) A single field-of-view of a FYLM device with  $4 \mu\text{m}$  catch channels. The entrance to the central trench is visible in the center, and the side trenches are on the left and right. Most catch channels captured individual viable *S. pombe* cells, and some cells have begun mitosis. Scale bar is  $20 \mu\text{m}$ . (bottom) Time-lapse images of the cell in the red box. Each row shows four time points in one mitotic cycle of the same cell. The catch channel holds the original cell in place, while new cells are washed away as they separate.

catch channel for tens of hours while the progeny cells are rapidly pushed out into the flow medium. Longer time-scale imaging revealed that individual cells within the FYLM continued to replicate for over 90 h (Video S2 (ac500893a\_si\_003.avi), Supporting Information). Figure 5 demonstrates that cells exhibited robust growth in the catch channels. The replication rate (Figure 5A) and cell length (Figure 5B) in the PDMS device is indistinguishable from doubling times and birth length of exponentially growing cells cultured in rich liquid media.<sup>42,43,25</sup> The cells divided every  $130 \pm 25$  min (mean  $\pm$  std. dev.;  $N = 139$  divisions); their birth length was  $7.1 \pm 0.9 \mu\text{m}$  (mean  $\pm$  std. dev.;  $N = 2250$ ). Importantly, the replication rate and cell morphology were not perturbed by the



**Figure 5.** (A) Histogram of cell division times ( $N = 139$  divisions). The cell division times are fit to a Gaussian distribution (red line, mean of 130 min with a standard deviation of 25 min). These results are in excellent agreement with the division time for wild type *S. pombe* in rich media (130–150 min),<sup>42,43</sup> indicating that the FLYM device is not impeding normal cell division (also see Figure S6, Supporting Information). (B) Histogram of old pole cell lengths immediately after division (“birth length”,  $N = 2250$  divisions). The red line is a fit to a Gaussian distribution (mean of  $7.1 \mu\text{m}$  with a standard deviation of  $0.9 \mu\text{m}$ ). These results are in agreement with other measurements of birth length for wild type *S. pombe* in rich media microcolonies ( $7.3 \pm 0.7 \mu\text{m}$ ).<sup>25</sup>

confinement within the catch channels and the continuous perfusion of fresh media (Figure S6 and Table S2, Supporting Information). Thus, we concluded that the FYLM provides an optimal growth environment for fission yeast.

We next observed the dynamics of protein aggregates in individual *S. pombe* cells. Proteotoxic stress is a key determinant of cellular longevity,<sup>44</sup> however, little is known about the accumulation and segregation of protein aggregates in fission yeast cells.<sup>9,10,44</sup> Misfolded proteins accumulate into larger intracellular clusters that colocalize with Hsp104, a protein-aggregate remodeling factor.<sup>9,45,46</sup> To observe protein aggregates, we fluorescently imaged the dynamics of Hsp104 fused to a C-terminal GFP.<sup>47</sup> The chromosomally encoded Hsp104-GFP was driven by its endogenous promoter and expressed within its native genetic locus.<sup>47</sup> *S. pombe* cells were loaded into the FYLM, and each field-of-view was sequentially imaged via epifluorescence and bright field microscopy.

As a proof-of-principle, we induced proteome-wide aggregation by treating the cells with hydrogen peroxide ( $\text{H}_2\text{O}_2$ ). First, cells were loaded into the FYLM and allowed to grow in the device for 4 h (Figure 6). After the cells had undergone at least one round of replication, the media was switched to YES +1 mM  $\text{H}_2\text{O}_2$  for 30 min (Figure 6A). As reported previously

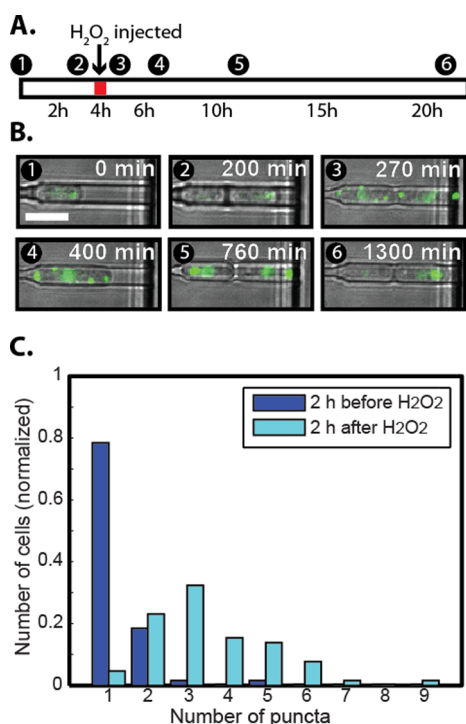


**Figure 6.** Hsp104-GFP relocalizes to distinct puncta after a proteotoxic (H<sub>2</sub>O<sub>2</sub>) stress. (A) Timeline of the experiment. First, cells are loaded into the FYLM and allowed to grow for 4 h. At the 4 h mark, YES+1 mM H<sub>2</sub>O<sub>2</sub> is injected into the device for 30 min. (B) Representative images of a single cell over the course of the experiment. Hsp104-GFP forms numerous puncta after exposure to YES+1 mM H<sub>2</sub>O<sub>2</sub>. These puncta coalesce to form larger bodies over the course of the experiment. (C) The number of Hsp104-GFP puncta increases in individual cells after an H<sub>2</sub>O<sub>2</sub> shock ( $N = 65$  cells). Two hours prior to H<sub>2</sub>O<sub>2</sub> injection, cells harbor  $1.0 \pm 0.9$  puncta. Two hours after exposure to H<sub>2</sub>O<sub>2</sub>, cells contain an average of  $3.5 \pm 1.6$  puncta. Statistical analysis of puncta in individual cells shows a significant difference before and after exposure ( $p = 3.3 \times 10^{-16}$ ).

in both *S. cerevisiae* and *S. pombe*, Hsp104-GFP rapidly reorganized into numerous small punctate foci that segregated between dividing cells.<sup>9,45</sup> Following H<sub>2</sub>O<sub>2</sub> treatment, cells entered cell-cycle arrest and significantly slowed their replication time (Figures 6B and 7). Surprisingly, the cells showed a persistent delay in their replication times for up to seven generations after the H<sub>2</sub>O<sub>2</sub> treatment (Figure 7). Importantly, we could continuously observe the dynamic movement of Hsp104-GFP foci over at least ten cell divisions (Video S3 (ac500893a\_si\_004.avi), Supporting Information). Together, these experiments demonstrate that the FYLM device permits wide-field fluorescence observation of Hsp104-GFP, a fluorescent reporter of proteome-wide misfolding. These results demonstrate that the FYLM will permit future studies to monitor key cellular senescence factors in precisely aged fission yeast cells.

## CONCLUSION

In this report, we describe long-scan  $\mu$ 3DP, a direct-write multiphoton lithography method capable of producing large aspect ratio, 3D structures with micrometer-scale features. This  $\mu$ 3DP method combines the flexibility of dynamic mask-based  $\mu$ 3D printing<sup>28,35,39</sup> with the millimeter-length scales achieved by previous raster-scan methods.<sup>37,38</sup>

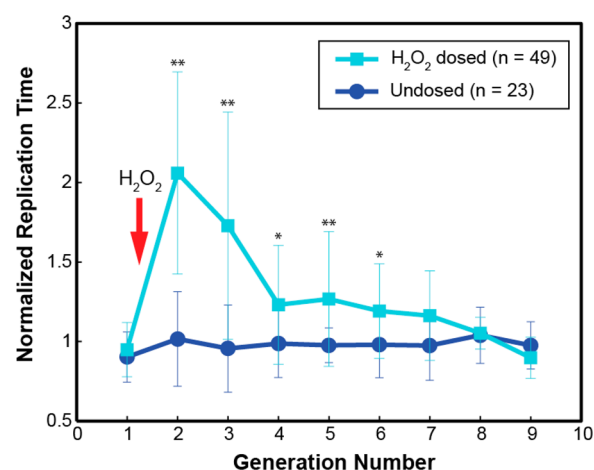


**Figure 7.** Normalized replication times following treatment with 1 mM H<sub>2</sub>O<sub>2</sub>. Cells are exposed to H<sub>2</sub>O<sub>2</sub> between the first and second generations (as shown by the arrow). Time required for replication doubles immediately after the proteotoxic stress. Cells begin to recover, showing a return to normal doubling times around generation 7 (6 generations after the stress). Error bars show standard deviation; asterisks denote a significant statistical difference between control population and dosed population: \*\* $p < 0.01$ , \* $p < 0.05$ .

Using  $\mu$ 3DP as a rapid prototyping method, we developed the FYLM, a high-throughput microfluidic platform for aging studies and long time-scale single-cell analysis in fission yeast. Microfluidic dissection offers a number of advantages over manual micromanipulation studies. Our devices are compatible with high-resolution time-lapse microscopy methods. Second, we can physically capture and observe a large cohort of individually addressable cells. As the cells are immobilized via gentle suction, no chemical modification of the cell wall is required.<sup>14</sup> Continuous flow of fresh growth medium ensures that all cells experience a similar nutrient environment. Most importantly, the identity of the aging cell pole is geometrically constrained and can be unambiguously identified in confined cells. Because mitochondrial maintenance and other aging-associated processes are conserved between fission yeast and metazoans, high-throughput studies in this eukaryotic model organism offer great potential for shedding light on many aspects of cellular aging.

In addition to its utility in the rapid prototyping of masters for PDMS molding,  $\mu$ 3DP can also be used to develop micrometer-scale devices that require intricate or unconventional geometries, such as curves or sloping/irregular top surfaces. Moreover,  $\mu$ 3DP can be used to fabricate structures from a range of biological materials, including proteins and other biocompatible substrates.<sup>33,35,39</sup> For example,  $\mu$ 3DP of a protein matrix has been used to produce bacterial micro-environments.<sup>36,48</sup> Thus, the long-scan  $\mu$ 3DP approach described in this report will allow the generation of novel, millimeter-scale 3D structures and devices.

## ASSOCIATED CONTENT

### Supporting Information

Additional information including detailed methods, six supplemental figures, and three videos. This material is available free of charge via the Internet at <http://pubs.acs.org>.

## ■ AUTHOR INFORMATION

## Corresponding Authors

\*E-mail: jshear@cm.utexas.edu.

\*E-mail: ifinkelstein@cm.utexas.edu

## Notes

The authors declare no competing financial interest.

## ■ ACKNOWLEDGMENTS

This research was supported in part by the Welch Foundation (F-1808 to I.J.F.; F-1331 to J.B.S.) and by startup funds from the University of Texas at Austin. I.J.F. is a CPRIT Scholar in Cancer Research. We thank Dr. Edward Marcotte and his research group for occasional use of their inverted fluorescence microscope. I.J.F., J.B.S., and B.X. are Fellows in the Institute of Cellular and Molecular Biology.

## ■ REFERENCES

- (1) Mortimer, R. K.; Johnston, J. R. *Nature* **1959**, *183*, 1751–1752.
- (2) Henderson, K. A.; Gottschling, D. E. *Curr. Opin. Cell Biol.* **2008**, *20*, 723–728.
- (3) McMurray, M. A.; Gottschling, D. E. *Curr. Opin. Microbiol.* **2004**, *7*, 673–679.
- (4) Sinclair, D. A. In *Biological Aging: Methods and Protocols (Methods in Molecular Biology)*; Tollefsbol, T. O., Ed.; Humana Press: Totowa, NJ, 2013; pp 49–63.
- (5) Sinclair, D. A. *Mech. Ageing Dev.* **2002**, *123*, 857–867.
- (6) Wasko, B. M.; Kaeberlein, M. *FEMS Yeast Res.* **2014**, *14*, 148–159.
- (7) Kenyon, C. J. *Nature* **2010**, *464*, 504–512.
- (8) Smith, E. D.; Tsuchiya, M.; Fox, L. A.; Dang, N.; Hu, D.; Kerr, E. O.; Johnston, E. D.; Tcho, B. N.; Pak, D. N.; Welton, K. L.; Promislow, D. E. L.; Thomas, J. H.; Kaeberlein, M.; Kennedy, B. K. *Genome Res.* **2008**, *18*, 564–570.
- (9) Coelho, M.; Dereli, A.; Haese, A.; Kühn, S.; Malinowska, L.; DeSantis, M. E.; Shorter, J.; Alberti, S.; Gross, T.; Tolić-Nørrelykke, I. M. *Curr. Biol.* **2013**, *23*, 1–9.
- (10) Erjavec, N.; Cvijovic, M.; Klipp, E.; Nystrom, T. *Proc. Natl. Acad. Sci. U.S.A.* **2008**, *105*, 18764–18769.
- (11) Barker, M. G.; Walmsley, R. M. *Yeast* **1999**, *15*, 1511–1518.
- (12) Lee, S. S.; Vizcarra, I. A.; Huberts, D. H. E. W.; Lee, L. P.; Heinemann, M. *Proc. Natl. Acad. Sci. U.S.A.* **2012**, *109*, 4916–4920.
- (13) Zhang, Y.; Luo, C.; Zou, K.; Xie, Z.; Brandman, O.; Ouyang, Q.; Li, H. *PLoS One* **2012**, *7*, No. e48275.
- (14) Xie, Z.; Zhang, Y.; Zou, K.; Brandman, O.; Luo, C.; Ouyang, Q.; Li, H. *Aging cell* **2012**, *11*, 599–606.
- (15) Terenna, C. R.; Makushok, T.; Velve-Casquillas, G.; Baigl, D.; Chen, Y.; Bornens, M.; Paoletti, A.; Piel, M.; Tran, P. T. *Curr. Biol.* **2008**, *18*, 1748–1753.
- (16) Minc, N.; Boudaoud, A.; Chang, F. *Curr. Biol.* **2009**, *19*, 1096–1101.
- (17) Wang, P.; Robert, L.; Pelletier, J.; Dang, W. L.; Taddei, F.; Wright, A.; Jun, S. *Curr. Biol.* **2010**, *20*, 1099–1103.
- (18) Tian, Y.; Luo, C.; Ouyang, Q. *Lab Chip* **2013**, *13*, 4071–4077.
- (19) Spivey, E. C.; Finkelstein, I. J. *Mol. BioSyst.* **2014**, *10*, 1658–1667.
- (20) Bell, L.; Seshia, A.; Lando, D.; Laue, E.; Palayret, M.; Lee, S. F.; Klenerman, D. *Sens. Actuators, B* **2014**, *192*, 36–41.
- (21) Grünberger, A.; Wiechert, W.; Kohlheyer, D. *Curr. Opin. Biotechnol.* **2014**, *29*, 15–23.
- (22) Minc, N.; Chang, F. *Curr. Biol.* **2010**, *20*, 710–716.
- (23) Casquillas, G. V.; Fu, C.; Berre, M. L.; Cramer, J.; Meance, S.; Plecis, A.; Baigl, D.; Greffet, J.-J.; Chen, Y.; Piel, M.; Tran, P. T. *Lab Chip* **2011**, *11*, 484–489.
- (24) Syrovatkina, V.; Fu, C.; Tran, P. T. *Curr. Biol.* **2013**, *23*, 2423–2429.
- (25) Nobs, J.-B.; Maerkl, S. J. *PLoS One* **2014**, *9*, No. e93466.
- (26) Xia, Y.; Whitesides, G. M. *Annu. Rev. Mater. Sci.* **1998**, *28*, 153–184.
- (27) Folch, A.; Ayon, A.; Hurtado, O.; Schmidt, M. A.; Toner, M. J. *Biomech. Eng.* **1999**, *121*, 28–34.
- (28) Ritschdorff, E. T.; Nielson, R.; Shear, J. B. *Lab Chip* **2012**, *12*, 867–871.
- (29) Maruo, S.; Nakamura, O.; Kawata, S. *Opt. Lett.* **1997**, *22*, 132–134.
- (30) Kawata, S.; Sun, H.-B.; Tanaka, T.; Takada, K. *Nature* **2001**, *412*, 697–698.
- (31) Kaehr, B.; Ertas, N.; Nielson, R.; Allen, R.; Hill, R. T.; Plenert, M.; Shear, J. B. *Anal. Chem.* **2006**, *78*, 3198–3202.
- (32) Maruo, S.; Fourkas, J. T. *Laser Photonics Rev.* **2008**, *2*, 100–111.
- (33) Jhaveri, S.; McMullen, J.; Sijbesma, R.; Tan, L.; Zipfel, W.; Ober, C. *Chem. Mater.* **2009**, *21*, 2003–2006.
- (34) Culver, J. C.; Hoffmann, J. C.; Poché, R. A.; Slater, J. H.; West, J. L.; Dickinson, M. E. *Adv. Mater.* **2012**, *24*, 2344–2348.
- (35) Spivey, E. C.; Ritschdorff, E. T.; Connell, J. L.; McLennon, C. A.; Schmidt, C. E.; Shear, J. B. *Adv. Funct. Mater.* **2013**, *23*, 333–339.
- (36) Connell, J. L.; Ritschdorff, E. T.; Whiteley, M.; Shear, J. B. *Proc. Natl. Acad. Sci. U.S.A.* **2013**, *110*, 18380–18385.
- (37) Kumi, G.; Yanez, C. O.; Belfield, K. D.; Fourkas, J. T. *Lab Chip* **2010**, *10*, 1057.
- (38) Liu, Y.; Nolte, D. D.; Pyrak-Nolte, L. J. *Appl. Phys. A: Mater. Sci. Process.* **2010**, *100*, 181–191.
- (39) Nielson, R.; Kaehr, B.; Shear, J. *Small* **2009**, *5*, 120–125.
- (40) Hayles, J.; Wood, V.; Jeffery, L.; Hoe, K.-L.; Kim, D.-U.; Park, H.-O.; Salas-Pino, S.; Heichinger, C.; Nurse, P. *Open Biol.* **2013**, *3*, 130053.
- (41) Navarro, F. J.; Nurse, P. *Genome Biol.* **2012**, *13*, R36.
- (42) Forsburg, S. L.; Rhind, N. *Yeast* **2006**, *23*, 173–183.
- (43) Sabatinos, S. A.; Forsburg, S. L. In *Methods in Enzymology, Guide to Yeast Genetics: Functional Genomics, Proteomics, and Other Systems Analysis*; Weissman, J., Guthrie, C., Fink, G. R., Eds.; Academic Press: New York, 2010; Vol. 470, pp 759–795.
- (44) Morimoto, R. I. *Genes Dev.* **2008**, *22*, 1427–1438.
- (45) Liu, B.; Larsson, L.; Caballero, A.; Hao, X.; Öling, D.; Grantham, J.; Nyström, T. *Cell* **2010**, *140*, 257–267.
- (46) Erjavec, N.; Larsson, L.; Grantham, J.; Nyström, T. *Genes Dev.* **2007**, *21*, 2410–2421.
- (47) Nilsson, D.; Sunnerhagen, P. *RNA* **2011**, *17*, 120–133.
- (48) Connell, J. L.; Wessel, A. K.; Parsek, M. R.; Ellington, A. D.; Whiteley, M.; Shear, J. B. *mBio* **2010**, *1*, e00202–10–e00202–17.